

Estimating Long GRB Jet Opening Angles and Rest-Frame Energetics

Adam Goldstein¹, Valerie Connaughton², Michael S. Briggs³, Eric Burns³

Received _____; accepted _____

¹Space Science Office, VP62, NASA/Marshall Space Flight Center, Huntsville, AL 35812, USA

²Science and Technology Institute, Universities Space Research Association, Huntsville, AL 35805, USA

³Center for Space Plasma and Aeronomic Research, University of Alabama in Huntsville, 320 Sparkman Drive, Huntsville, AL 35899, USA

ABSTRACT

We present a method to estimate the jet opening angles of long duration Gamma-Ray Bursts (GRBs) using the prompt gamma-ray energetics and an inversion of the Ghirlanda relation, which is a correlation between the time-integrated peak energy of the GRB prompt spectrum and the collimation-corrected energy in gamma rays. The derived jet opening angles using this method and detailed assumptions match well with the corresponding inferred jet opening angles obtained when a break in the afterglow is observed. Furthermore, using a model of the predicted long GRB redshift probability distribution observable by the *Fermi* Gamma-ray Burst Monitor (GBM), we estimate the probability distributions for the jet opening angle and rest-frame energetics for a large sample of GBM GRBs for which the redshifts have not been observed. Previous studies have only used a handful of GRBs to estimate these properties due to the paucity of observed afterglow jet breaks, spectroscopic redshifts, and comprehensive prompt gamma-ray observations, and we potentially expand the number of GRBs that can be used in this analysis by more than an order of magnitude. In this analysis, we also present an inferred distribution of jet breaks which indicates that a large fraction of jet breaks are not observable with current instrumentation and observing strategies. We present simple parameterizations for the jet angle, energetics, and jet break distributions so that they may be used in future studies.

Subject headings: gamma rays: bursts — methods: data analysis

1. Introduction

A key to understanding the progenitors and central engines of Gamma-Ray Bursts (GRBs) is to know the total energy budget of these enormous stellar explosions. One way to estimate the total kinetic energy in a GRB is to calculate the amount of energy radiated in gamma rays and estimate the efficiency of converting the energy in the mass outflow of the explosion to the radiated energy that is observed (Frail et al. 2001; Freedman & Waxman 2001; Ghisellini et al. 2002). Several factors affect the apparent radiated energy such as the physics of the mass-radiation conversion and the Lorentz factor of the relativistic jet (Kumar & Piran 2000). These properties are difficult to estimate and are not observed directly. In most cases even the radiated energy of a GRB is not readily estimated, since it requires a broadband gamma-ray modeling of the prompt emission, a set of comprehensive broadband observations of the afterglow to estimate the amount of jet collimation (Sari et al. 1999; Frail et al. 2001), and optical identification of the redshift (Bloom et al. 1998). The myriad of requisite observations and inferences to estimate the radiated energy in gamma rays has provided robust energetics estimates for only a few tens of GRBs compared to the several thousand GRBs that have been detected.

One particular physical property of GRBs that has a large impact on the observed energetics is the degree to which the jetted outflow is collimated. The amount of collimation in a particular GRB can adjust the inferred rest-frame energy or luminosity several orders of magnitude from an assumed isotropic explosion. For this reason, the jet opening angle of GRBs is an important property to measure if inferences are to be made about their rest-frame energetics. Unfortunately, the jet opening angle is difficult to reliably estimate, since it requires observations of an achromatic jet break in the power-law decay of the afterglow emission, most often observed in the optical and X-ray bands (Sari et al. 1999; Harrison et al. 1999; O’Brien et al. 2006). In all but a small number of cases these

observations are complicated by limited observations of the afterglow, rapidly fading afterglow, and late-time X-ray flaring variability in the afterglow (Costa 1999; O’Brien et al. 2006). In addition to the jet break time, observations of the host environment and detailed afterglow spectroscopy are generally needed to estimate the particle density profile of the surrounding circumburst medium to estimate the jet opening angle (Waxman 1997; Wijers & Galama 1999). Because of these difficulties, there are currently only ~ 50 GRBs with reasonably constrained jet breaks and ~ 20 of those GRBs have reasonable constraints on the circumburst density profile. An additional complication is that many of the GRBs with constrained jet breaks do not have the broad prompt spectral coverage necessary to adequately calculate the flux and fluence as measured in gamma rays.

Using the available small samples of GRBs with adequate observations, a number of observed correlations between GRB spectral or temporal observables and the rest-frame energetics of the explosion have been discovered (Norris et al. 2000; Amati et al. 2002; Ghirlanda et al. 2004; Yonetoku et al. 2004; Guidorzi et al. 2006), and they have been used to investigate the physics of the prompt emission of GRBs. Some of these correlations have large dispersion, in many cases too large for meaningful physical inference from the correlation. One particularly tight correlation is between the rest-frame peak energy of the time-integrated prompt GRB spectrum and the collimation-corrected rest-frame energy in gamma rays, known as the Ghirlanda relation (Ghirlanda et al. 2004). We endeavor to empirically estimate the jet opening angle for GRBs from the prolifically observed prompt gamma-ray emission by inverting the Ghirlanda relation. As previous works have shown (Ghirlanda et al. 2005a, 2013) this method can alleviate the problems associated with the scarcity and difficulty of obtaining simultaneous measurements over several energy regimes.

As we will show, the inversion of the Ghirlanda relation to estimate the jet opening

angle requires knowledge of the GRB redshift, but only a small fraction ($<10\%$) of observed GRBs have an observed redshift. Current observations of redshift are biased toward GRBs that are observed and localized by *Swift*, which has a gamma-ray bandpass that is typically too low to capture the curvature in the GRB spectrum, thereby biasing the estimate of the rest-frame gamma-ray energetics of the GRB. Because of the very small fraction ($\approx 1\%$) of all GRBs with both known redshift and broadband gamma-ray observations, there have been multiple investigations to use observed spectral and temporal correlations to predict the redshift (Atteia 2003; Yonetoku et al. 2004; Ghirlanda et al. 2005a; Amati 2006). The accuracy of these methods are difficult to assess and are fraught with systematic biases and large uncertainties (Goldstein et al. 2012a). We propose to avoid this complication by using the estimated redshift probability distribution of long GRBs that is observable by a particular instrument—in this case, the *Fermi* Gamma-ray Burst Monitor (GBM). The redshift distribution is applied as our prior knowledge when the redshift has not been directly observed. This allows us to estimate the probability density functions (PDFs) for the rest-frame energetics of individual GRBs without known redshift as well as estimates on the population distributions of energetics.

2. Methodology

2.1. The Ghirlanda Correlation & Jet Opening Angles

Estimates of the energy and luminosity require an implicit assumption about the cosmological expansion of the universe. To avoid the uncertainty in assuming a cosmological model, we follow the procedure of Liang et al. (2008) by using the correlation between the redshift and distance (known as the Hubble Diagram) for Type Ia Supernovae (SNe Ia) to directly estimate the distance to GRBs with $z < 1.5$. Since the distance of SNe Ia are well-estimated by standard lightcurve-fitting techniques, they provide a calibration

sample for GRBs that overlap in redshift. In general, the SNe Ia Hubble Diagram can be interpolated to find the distance for a given redshift. The uncertainty in the interpolation can then be propagated to represent the uncertainty in the distance of the GRB. This procedure produces a model-independent estimation of the luminosity distance for GRBs to be used in the calculation of the source energetics.

Using this method to estimate the luminosity distance, we collect a sample of GRBs with $z < 1.5$ that have observed and published jet break time estimates. The jet break time, redshift, and spectral properties used for these bursts are included in Table 1. Most GRBs in the table are fit with the traditional empirical Band function (Band et al. 1993), with the GRBs for which there is no high-energy index, β , in the table modeled with an exponentially cut-off power law. Using the fluence and redshift of each GRB, the isotropic energy, E_{iso} can be calculated. Because spectral and fluence measurements of the sample are from different instruments with different bandpasses, and due to the cosmological shifting of the spectral bandpass into the rest-frame of the GRB, the spectral parameters in Table 1 are used to calculate the cosmological K-correction as prescribed in Bloom et al. (2001). The isotropic energy is then calculated as

$$E_{\text{iso}} = \frac{4\pi d_L^2 S_\gamma K(z; F(E))}{1+z}, \quad (1)$$

where d_L is the luminosity distance, S_γ is the fluence in the detector band, and $K(z; F(E))$ is the K-correction used to scale the fluence from the observed detector band to some consistent rest-frame band. In this paper, we calculate the K-correction for a rest-frame energy band of 1 keV–10 MeV.

Under the assumption of the standard afterglow model and a simple uniform jet, the jet opening angle, θ_j , can then be estimated from the measured jet break time, t_j , as

$$\theta_j \approx 0.057 \left(\frac{t_j}{1 \text{ day}} \right)^{3/8} \left(\frac{1+z}{2} \right)^{-3/8} \left(\frac{E_{\text{iso}}}{10^{53} \text{ erg}} \right)^{-1/8} \left(\frac{\epsilon}{0.2} \right)^{1/8} \left(\frac{n_p}{0.1 \text{ cm}^{-3}} \right)^{1/8}, \quad (2)$$

where ϵ is an estimate of the efficiency in converting the bulk kinetic outflow into gamma rays, and n_p is the circumburst density (Sari et al. 1999; Frail et al. 2001). Both ϵ and n_p are largely unknown, although some rare measurements of n_p have been made, and ϵ is typically assumed to be 20%. In this work, we assume that the ϵ and n_p are not specifically known for each GRB. For ϵ , we assume a broad uniform distribution spanning 5%–95%, consistent with estimates of GRB radiative efficiencies that span from $< 10\%$ to $> 90\%$ (Zhang et al. 2007). We assume a log-normal distribution for n_p with mean $\log_{10}(0.1)$ and standard deviation 1.0, which is derived from the distribution of the small number of measured n_p . As can be seen from Equation 2, θ_j is less dependent on ϵ and n_p than on the jet break time. Since the parameter uncertainties may not be strictly Gaussian, we calculate the uncertainty in θ_j by Monte Carlo sampling from the respective parameter probability density functions and repeatedly use Equation 2 to build up the probability distribution for θ_j .

Having calculated θ_j , the collimation-corrected energy is defined by

$$E_\gamma = E_{\text{iso}}[1 - \cos(\theta_j)]. \quad (3)$$

The peak of the νF_ν spectrum, known as E_{peak} , in the rest-frame, $E_{p,z}$, can then be plotted against E_γ , which shows the observed Ghirlanda relation, displayed in Figure 1. The estimated best fit for the power law using a Bayesian method taking into account uncertainties in both variables and intrinsic scatter (Kelly et al. 2007) is:

$$\frac{E_{p,z}}{1 \text{ keV}} = 10^{2.57 \pm 0.08} \left(\frac{E_\gamma}{3.8 \times 10^{50} \text{ erg}} \right)^{0.61 \pm 0.10}. \quad (4)$$

The correlation index is in good agreement with the 2/3 prediction of Levinson & Eichler (2005), in which the $E_{p,z} - E_\gamma$ correlation was derived using jet dynamics and off-axis viewing effects of a simple annular jet and is consistent with previous findings (Ghirlanda et al. 2007). Figure 1 also displays the $E_{p,z} - E_\gamma$ correlation for a sample of GRBs at high redshift

($z > 1.5$). The correlation at higher redshift is generally consistent with the the calibrated correlation and the parameters used for these GRBs can be found in Table 2. When using values of redshift at $z > 1.5$, we assume the concordant Λ CDM cosmology with $\Omega_M = 0.27$, $\Omega_\Lambda = 0.73$, and $H_0 = 70 \text{ km Mpc}^{-1} \text{ s}^{-1}$.

Using Equations 1, 3, and 4, the correlation can be inverted to estimate θ_j given the time-integrated observed spectrum, fluence, and redshift:

$$\theta_j = \cos^{-1} \left(1 - \frac{3.8 \times 10^{50}}{4\pi} \frac{1+z}{d_L^2 S_\gamma K} \left[\frac{E_{\text{peak}}(1+z)}{\xi} \right]^{1/\eta} \right), \quad (5)$$

where $\xi = 10^{2.57 \pm 0.08}$ and $\eta = 0.61 \pm 0.10$ are the correlation amplitude and index, respectively. We choose to calculate the uncertainties on θ_j via Monte Carlo sampling of d_L , S_γ , K , E_{peak} , ξ , and η . We do this because the PDFs for each of these quantities are not necessarily Gaussian or even symmetric, and this method is further required when the redshift is not explicitly known, as discussed in the next section.

2.2. Redshift Distribution of GRBs Observable by GBM

The GBM-observable GRB redshift distribution can be estimated by taking into account the detector sensitivity, the detector-dependent GRB luminosity function, and the GRB rate density evolution. We follow this method detailed in Coward et al. (2013), who used the method to produce the redshift distribution for *Swift* GRBs. Specifically, the GRB redshift distribution observable by GBM can be written as

$$P(z) = N_p \frac{dV(z)}{dz} \frac{e(z)}{1+z} \psi_{\text{GBM}}(z), \quad (6)$$

where $dV(z)/dz$ is the comoving cosmological volume element, $e(z)$ is the GRB rate evolution model, $\psi_{\text{GBM}}(z)$ is the GBM sensitivity to detecting GRBs at redshift z , and N_p is the normalization. Coward et al. (2013) showed that when a complete sample of

observed *Swift* GRBs with redshift was studied factoring in the *Swift* detector biases as well as detailed optical biases that affect the observation of redshift, neither luminosity nor density evolution for GRBs was required to explain the observed GRB rate deviation from the star formation rate. Therefore $e(z)$ represents a parametrization of the star formation rate that is normalized to the local GRB rate density. ψ_{GBM} is calculated by estimating the detector- dependent luminosity function and integrating it over observable luminosities. Following Howell & Coward (2013), we use an exponentially cut-off power law to model the luminosity function of GBM GRBs:

$$\phi(L) = \phi_0 \left(\frac{L}{L_*} \right)^\alpha \exp\left(-\frac{L}{L_*} \right), \quad (7)$$

where ϕ_0 is the normalization and the best fit parameters from the differential log N–log P distribution is $L_* = (4.66^{+0.09}_{-0.48}) \times 10^{52}$ erg s^{−1} and $\alpha = -4.03^{+0.16}_{-0.05}$. Note that these parameters are consistent with Howell & Coward (2013) and the no-evolution model in Salvaterra & Chincarini (2007) for *Swift* GRBs. The luminosity function is integrated starting at a lower-limiting luminosity defined by the lowest peak flux observed:

$$\psi_{GBM}(z) = \int_{L_{\text{lim}}(F_{\text{lim}},z)}^{L_{\text{max}}} \phi(L)dL, \quad (8)$$

where L_{lim} is the limiting luminosity, which is a function of the limiting flux, F_{lim} (0.8 ph s^{−1} cm^{−2} in 10–1000 keV for GBM), and z . The observable redshift distribution is shown in Figure 2 and is compared to the distribution of long GRBs with measured spectroscopic redshift through March 2015 (Greiner 2015). The distribution of 40 GBM GRBs from the published four-year GBM Catalog (Gruber et al. 2014) with observed redshift is also compared against the theoretical redshift distribution. The obvious difference between the redshift distribution for observed GBM GRBs and the theoretical observable redshift distribution may be explained by the requirement that either the *Swift* BAT must have observed the GRB or that the GRB was particularly bright and seen in the *Fermi* LAT. Indeed, if Equation 6 is fit to the observed GBM redshift distribution, the resulting

limiting flux increases more than an order of magnitude to $F_{\text{lim}} = 10.5$, indicating that redshift observations for GBM GRBs is biased toward brighter bursts. Because the energy range, exposure, and sensitivity of instruments required to observe the prompt emission of a GBM burst and trigger follow-up observations are different from that of GBM, the current observed distribution of redshifts for GBM-detected GRBs is not guaranteed to be consistent with the true redshift distribution of all GRBs detected by GBM.

2.3. Estimation of Histograms

The jet opening angle and energetics distributions for GRBs without known redshift are constructed from probability distributions of the values in question that are much broader than if the individual redshift values are known. For this reason, binning the distributions requires some care. Typically histograms are produced by binning continuous data and the resulting bins are treated as a Poisson random variable, and therefore, for the n_i items in the i th bin, the (1σ) uncertainty is modeled as $\sqrt{n_i}$. This assumption is not appropriate for some of the distributions in this paper. Instead, we choose to create histograms via a Monte Carlo sampling from the PDF of each quantity from each GRB. Specifically, for a quantity of interest from N total GRBs in our sample, we first determine the edges of our bins, then we take a sample from each of the N PDFs and place them in the corresponding bins. This is done for a number of iterations (typically > 1000), randomly sampling from the PDFs and recording the counts in each bin for each iteration. This process creates a PDF for each bin of the histogram, from which we choose the median as the centroid of the bin and the error bars represent the 68% credible interval centered at the median. This Monte Carlo sampling method allows us to more accurately represent the underlying distribution, especially at the extremes of the distribution where a combination of several low probability densities can produce a non-negligible probability density in the histogram.

This method is applied to the histograms presented in the following section.

3. Data Analysis & Results

To study the rest-frame energetics we use the results from the *Fermi* GBM GRB spectroscopy catalog (Gruber et al. 2014), which covers the first four years of GBM observations. The catalog contains both the time-integrated spectral fits and the spectral fits at the peak flux for each of 943 GRBs. We only consider those GRBs which are defined as long by the centroid of the T_{90} duration estimate, namely $T_{90} > 2$ s. To obtain a reliable estimate of E_{peak} , we only consider long GRBs from that catalog which are adequately fit by the empirical Band function or an exponentially-cutoff power law, known as a Comptonized function. Specifically, we first consider long GRBs from the catalog that are well fit by a Band function with well-constrained parameters which results in 381 GRBs (the GOOD criteria defined in Gruber et al. (2014)). Of the remaining long GRBs, we add to our sample GRBs that are well fit by the Comptonized function as specified in the catalog, which results in an additional 257 GRBs. We use this sample of 638 long GRBs to study the θ_j and energetics distributions.

The following subsections describe the estimation of θ_j from the inversion of the Ghirlanda relation for GRBs with and without known redshift. This estimation of θ_j , particularly for GRBs without known redshift, is then applied to calculate the distributions of the rest-frame energetics. We also look at the correlations between three E_{peak} correlations: $E_{p,z} - E_{\text{iso}}$, $E_{p,z} - L_{\text{iso}}$, and $E_{p,z} - L_{\gamma}$. Finally, we present an estimate of the jet break time distribution which allow us to make predictions about the likelihood of directly observing jet breaks. Note that all of the PDFs that are generated are well modeled as log-normals. We parametrize the log-normal PDFs as $P(\log_{10} x) = N(\mu, \sigma)$ so that the μ and σ values quoted are for a normal distribution in \log_{10} space. The best-fit parameters

for the jet angle, energetics, and jet break time distributions can be found in Table 3. The log-normal parameters for all estimated quantities for each GRB in the GBM sample are listed in machine-readable format which is described in Table 4.

3.1. Predicting Jet Opening Angles

For GRBs with observed redshift, θ_j can be estimated by Equation 5. An important, but often ignored, aspect of this estimation is a proper propagation of uncertainty. We propagate the uncertainty in the fluence, E_{peak} , K-correction, luminosity distance, and the correlation parameters to estimate the uncertainty in θ_j for this method. A comparison of the inferred jet opening angle using the measured jet break and the estimate of the jet opening angle from this paper is shown in Figure 3(a). We find that 84% of the estimates for θ_j are consistent with the calculation of θ_j via observed jet breaks within the combined 1σ confidence level. Our propagation of uncertainty is shown to capture the uncertainty in the spectral fit and the Ghirlanda correlation.

Next, we test the method by comparing the same sample of GRBs with measured jet breaks to estimates of the θ_j derived assuming that we have not observed the redshift. In this case, we sample from the GRB redshift distribution described by Equation 6 and calculate the PDF for θ_j for each GRB. Figure 3(b) shows that our estimation of θ_j is again largely consistent with the jet break estimates of θ_j . In the case of unknown redshift, the uncertainty on θ_j should be larger, and this is reflected in the comparison. Also shown in Figure 3(c) is the estimated θ_j from the sample of 40 GBM GRBs with observed redshift compared to the estimation of θ_j assuming the redshift for those GRBs are unknown. The comparisons are consistent, with a larger uncertainty in θ_j when the redshift is assumed unknown, as expected. The centroids of the low- z GRBs all lie below the line of unity due to the fact that they all have redshifts below the peak of the redshift distribution in

Figure 2. Shown in Figure 3(d) is the dependence of θ_j on redshift for a given observation of E_{peak} and fluence, therefore a lower (higher) actual redshift for a given set of parameters would cause the derived θ_j to be higher (lower) than the estimate without knowledge of the redshift. One should note that the 1σ errors of the θ_j estimates describe the θ_j PDFs, which contain the full uncertainty from the redshift distribution.

Similarly, the θ_j PDFs can be calculated for each of the GRBs in our GBM sample. The PDFs are closely modeled as log-normal distributions and can be readily collected to form the largest sample to date to estimate the distribution of jet opening angles. Figure 4(a) shows the histogram of θ_j for the GBM sample and the log-normal fit to the distribution. The distribution of θ_j inferred from measured jet breaks is shown for comparison. As has been previously speculated, most long GRBs have highly collimated jets with opening angles $< 10^\circ$ (Frail et al. 2001; Bloom et al. 2003; Guetta et al. 2005), and our distribution shows that most GRBs indeed have $\theta_j < 10^\circ$. In fact, by our estimation, 90% of long GRB jet angles are $< 20^\circ$. On the other end of the distribution, we estimate that $\sim 2\%$ of opening angles are $< 1^\circ$. Figure 4(b) shows an average example of the PDF for an individual θ_j estimate. Our distribution for θ_j is consistent with that found by Ghirlanda et al. (2005a), where the distribution was also found to peak at $< 10^\circ$ and very few $> 50^\circ$.

There are particular selection effects that can lead to truncation of our estimated distribution of θ_j , primarily the limiting flux and fluence sensitivity of the detector and the potential existence of E_{peak} outside the GBM bandpass. For example, we do not attempt to estimate θ_j for GRBs that have a poorly constrained E_{peak} or are generally too weak to be fit by a Band or Comptonized function. Equation 5 shows that θ_j will generally increase with decreasing fluence and increase with increasing E_{peak} . In Figure 5 we show the correlations between our estimates of θ_j for the GBM sample and the fluence and E_{peak} for each GRB. The lowest fluence in 10-1000 keV for the GRBs fit with a Band

function is 9×10^{-7} erg cm $^{-2}$, while the least fluent from the Comptonized function is 4×10^{-7} erg cm $^{-2}$. The GRBs in the GBM catalog that can only be well-fit by a power law range in fluence from $3 \times 10^{-7} - 4 \times 10^{-5}$ erg cm $^{-2}$, therefore it is unlikely that the low fluence from the simple power-law fits alone would cause the GRBs that we disregarded to have significantly different jet angles. It is also unlikely because a regression indicates that θ_j would approach 90° at one to two orders of magnitude lower fluence than what has been observed with GBM. Alternatively, Figure 5(b) shows that an E_{peak} that has been redshifted below the GBM bandpass could indicate that $\theta_j < 1^\circ$. GBM has observed a handful of GRBs with $E_{\text{peak}} > 1$ MeV, but none have been observed to approach the 40 MeV upper bound of the detector band. A regression indicates that an E_{peak} above 40 MeV would likely approach a jet angle of 90° .

In addition to observational selection effects, changes to our assumed GRB redshift distribution can affect the estimated θ_j distribution. We have found that minor changes to the GRB redshift model do not significantly affect our θ_j and energetics distributions. For example, the difference between the redshift distribution used in this paper and the redshift distribution derived for *Swift* in Coward et al. (2013) produces a difference of $\sim 0.1^\circ$ in the peak of the θ_j distribution and no change in the width. Additionally, we produced θ_j estimates from the redshift model that we fitted to the observed GBM redshift distribution (blue dashed line in Figure 2). The θ_j estimates using this redshift distribution changed by an average of 12% or 0.4σ compared to our preferred redshift distribution. This causes a 0.5° shift in the peak of the ensemble θ_j distribution in Figure 4(a). These comparisons show that this method of estimating θ_j is robust and is insensitive to moderate changes in the assumed redshift distribution.

3.2. Rest-Frame Energetics

Similar to the estimation of the θ_j PDFs for GRBs by sampling from the GBM-observable redshift distribution, we can estimate the E_{iso} PDFs (1 keV–10 MeV) for our sample of GBM GRBs. Additionally, we can use our estimates of θ_j for each GRB to produce PDFs for the collimation-corrected energy, E_γ . In this case, we sample from the joint redshift– θ_j distribution to accurately calculate the E_γ PDF. In practice, we first sample from the redshift distribution, and then we sample from the θ_j distribution conditional on the sampled redshift. Using this process, we estimate the E_{iso} and E_γ PDFs for our GBM sample and construct the histograms, shown in Figure 6. Our results show that the E_{iso} distribution is broader than the E_γ distribution, although we show that E_γ likely spans 4 orders of magnitude and appears to have an interesting non-Gaussian high-energy tail. The distribution of E_{iso} appears to peak at $\sim 1 \times 10^{53}$ erg and has relatively few events at $> 1 \times 10^{55}$ erg, which places the most energetic observed GRB to date, 080916C (Abdo et al. 2009), at the 98th percentile of all likely events. Using the estimated jet break from Maselli et al. (2014) for the brightest observed GRB 130427A, $E_\gamma \approx 7 \times 10^{50}$ erg, which is only at the 46th percentile of our distribution. However, the famous ‘naked eye’ burst 080319 (Racusin et al. 2008) is estimated to currently have the largest collimation-corrected bolometric gamma-ray energy (1 keV–10 MeV) at $\approx 1 \times 10^{52}$ erg, based on the Konus-Wind gamma-ray data (Golenetskii et al. 2008), which is at ~ 98 th percentile for the E_γ distribution. Our distribution of E_{iso} is broadly consistent with previous observations (Frail et al. 2001; Ghirlanda et al. 2004; Amati 2006; Nava et al. 2012). Our E_γ distributions are also similar to the observations from Frail et al. (2001) and Ghirlanda et al. (2004).

We perform the same calculations to estimate the peak luminosity distributions, L_{iso} and L_γ , as we did for the rest-frame energy. In these calculations, instead of using the

time-integrated spectrum for each GRB, we use the spectrum at the 1 s peak of each GRB. Because the spectrum at the peak of the GRB is not always as well constrained as the time-integrated spectrum, there are a number of GRBs in our GBM sample that do not have either an acceptable Band or Comptonized fit, and so we do not include those GRBs in the luminosity estimations. In total there are 445 GRBs (311 Band and 134 Comptonized) from the GBM sample that have estimated peak luminosities. Our estimated distributions of L_{iso} and L_{γ} are shown in Figure 7. Similar to what we find with the rest-frame energy, L_{γ} has a narrower distribution than L_{iso} , which is due to the fact that there exists a distribution of θ_j . Our distributions suggest that while isotropic peak luminosities may approach and exceed 10^{55} erg s $^{-1}$ in some cases, the actual rest-frame peak luminosity when corrected for collimation rarely exceeds 10^{52} erg s $^{-1}$. The L_{iso} distribution presented here is in good agreement with the distribution presented in Nava et al. (2012). We estimate that 130427A, although likely the brightest GRB observed to date, is only in the top third in isotropic luminosity and near the median in L_{γ} .

Many studies have looked at estimating the E_{peak} distribution in the rest-frame, investigating if there is a particular energy at which the intrinsic spectrum peaks (Mallozzi et al. 1995; Schaefer 2003; Liang & Dai 2004; Collazzi et al. 2011). We can add to this investigation by estimating the rest-frame distribution of E_{peak} . Figure 8 shows the distributions of the time-integrated $E_{p,z}$ and $E_{p,z}$ at the peak of the GRB. The distributions generally peak between 500–600 keV and have slightly non-Gaussian high-energy tails, which may hint at a truncation of the $E_{p,z}$ distribution, particularly at low energy. The low-energy end of our distributions imply that the GBM bandpass would impose restrictions on the observed distributions for GRBs at $z \gtrsim 9$. The paucity of GRBs with $E_{p,z} > 10$ MeV indicates that the upper threshold of the GBM band does not impose a restriction on observed E_{peak} , due to the fact that a higher energy $E_{p,z}$ would imply a larger energy and luminosity and would be even more likely to be observed by GBM than

sub-MeV $E_{p,z}$. The $E_{p,z}$ distributions are broadly interpreted as being defined by both the emission physics within the jet and the bulk Lorentz factor which blue-shifts the $E_{p,z}$ from the comoving jet frame to the cosmological rest-frame. The spread in the distributions may be attributed primarily to the differences in magnetic field strength and dynamics and to the distribution of bulk Lorentz factors among the GRBs (Baring & Braby 2004; Burgess et al. 2014).

Finally, to quantify the accuracy of the estimation of the rest-frame energetics employing the Ghirlanda relation and a proposed redshift distribution, we compare our estimates of the energetics to the sample of calibration GRBs in Tables 1 and 2. Out of the 37 GRBs in our calibration sample, 59% (97%) are consistent within 1σ (2σ) for the estimation of E_{iso} , 65% (95%) are consistent within 1σ (2σ) for the estimation of E_γ , and 68% (100%) are consistent within 1σ (2σ) of the time-integrated $E_{p,z}$. Similar numbers are found in the comparison with the luminosity. These comparisons indicate that our method provides accurate estimates that are well-calibrated to the calculation of the energetics for GRBs with known redshift.

3.3. Correlations

Now that we have calculated the rest-frame energy, luminosity, and E_{peak} , we investigate a few of the rest-frame correlations that have been discussed in literature. We use the large number of GRBs from our GBM sample to plot the time-integrated $E_{p,z} - E_{iso}$ (Amati et al. 2002), the peak $E_{p,z} - L_{iso}$ (Yonetoku et al. 2004), and the peak $E_{p,z} - L_\gamma$ (Ghirlanda et al. 2005b) correlations, shown in Figure 9. We fit each correlation with a power law to find the best-fit normalization and power-law index. Note that significant outliers to the correlations are likely to be GRBs that are at the extreme tails of the redshift distribution in Figure 2.

For the Amati relation, using the large sample of GRBs without known redshift, we find the best fit correlation to be

$$\frac{E_{p,z}}{1 \text{ keV}} = 10^{2.71 \pm 0.01} \left(\frac{E_{\text{iso}}}{1.41 \times 10^{53} \text{ erg}} \right)^{0.44 \pm 0.02}. \quad (9)$$

We compare this to the best-fit power law for the GBM GRBs with known redshift, which gives an index of 0.40 ± 0.05 . The power law indices from both samples are consistent with each other and are roughly consistent (within $2 - 3\sigma$) with the theoretical prediction of Levinson & Eichler (2005) of $1/2$ from simple annular jet dynamics and viewing angle effects. It is apparent that the correlation has a large dispersion, even when accounting for uncertainties, which makes it difficult to use to study cosmology as has been previously discussed (Nakar & Piran 2005; Band & Preece 2005; Collazzi et al. 2012).

A more narrow correlation is the peak $E_{p,z} - L_{\text{iso}}$ correlation, which we find is best fit by the power law

$$\frac{E_{p,z}}{1 \text{ keV}} = 10^{2.83 \pm 0.02} \left(\frac{L_{\text{iso}}}{7.5 \times 10^{52} \text{ erg s}^{-1}} \right)^{0.45 \pm 0.02}. \quad (10)$$

We find the correlation slope is less steep than, but close to, ~ 0.5 that was first fit by Yonetoku et al. (2004). The best-fit correlation using the GBM redshift GRBs gives an even shallower index of 0.36 ± 0.1 but is consistent with the larger distribution at 1σ . It is also interesting to note that three of the GRBs with known redshift that exist at low-luminosity compared to the sample of unknown redshift have an associated supernova: GRBs 081007 (Zhi-Ping et al. 2013), 091127 (Cobb et al. 2010), and 101219B (de Ugarte Postigo et al. 2011).

We also find that the tightest of the three correlations is the peak $E_{p,z} - L_{\gamma}$ correlation, which is best described as

$$\frac{E_{p,z}}{1 \text{ keV}} = 10^{2.83 \pm 0.01} \left(\frac{L_{\gamma}}{2.4 \times 10^{50} \text{ erg s}^{-1}} \right)^{0.43 \pm 0.01}. \quad (11)$$

Ghirlanda et al. (2005b), using a small sample of 16 GRBs with $E_{p,z}$ and L_γ , found a correlation slope of 0.56. We find, using the GBM redshift sample, that the index is 0.41 ± 0.10 , which is also inconsistent with the findings of Ghirlanda et al. (2005b). The differences may originate from the small sample size in Ghirlanda et al. (2005b) and in the fact that they fit the correlation only considering the scatter in L_γ instead of the scatter perpendicular to the power law fit. It is also worth noting that three GRBs that have significant scatter from the correlation are the two SN-associated low-luminosity GRBs 081007 and 091127 and the high-luminosity GRB 090902B (Abdo et al. 2009b), which has an additional power law spectral component spanning from keV to GeV.

3.4. Jet Break Time Distribution

In addition to estimating the rest-frame collimation and energetics of a large sample of GRBs, we can use our estimates of θ_j and E_{iso} to estimate the jet break time, t_j , for each GRB and uncover the distribution for t_j . We invert Equation 2 and calculate t_j using the same assumed distributions for ϵ and n_p as previously mentioned, and use Monte Carlo sampling of all PDFs in the equation. The resulting distribution of t_j is shown in Figure 10. Most jet breaks have been observed from ~ 0.5 –10 days after the prompt emission. Our distribution suggests that 90% of observed jet break times can vary by ~ 3 orders of magnitude, and a large fraction of jet breaks will not be observable. If only *Fermi* observes the prompt emission of GRB, typically a detection by the *Fermi* LAT is required to trigger X-ray observations of the afterglow. Since the LAT usually requires ~ 12 hours to confirm detection and localize a GRB, this is the earliest that the afterglow for a *Fermi* GRB would be observed. Based on our t_j distribution, we estimate that $\sim 10\%$ of GRBs have jet breaks that are within 12 hours after the prompt emission and are unlikely to be observed if only *Fermi* has observed the prompt emission. If *Swift* triggers on a GRB, the

observed jet break distributions presented in Racusin et al. (2009) imply that the X-ray Telescope on *Swift* can observe the jet break less than an hour after the prompt emission. We estimate that only $\sim 1\%$ of jet breaks will occur less than an hour after the prompt emission, although in these cases it is important to have enough rapid afterglow before the jet break to adequately constrain the fit to the break. The difficulties of observing rapid jet break affects only a small fraction of GRBs, but the situation at the high end of the t_j distribution is more problematic. We find that $\sim 44\%$ of GRBs will have $t_j > 10$ days and $\sim 13\%$ of GRBs will have $t_j > 100$ days. At these timescales, the afterglow flux will typically have faded below most X-ray and optical detector sensitivities and will be undetectable. If an average -1 power-law decay in time is assumed for the X-ray and optical afterglow, then our t_j distribution implies that an improvement of $\sim 1 - 2$ orders of magnitude in sensitivity is required to observe 85% of all jet breaks.

Based on Figure 10, we estimate that at best only $\sim 50\%$ of GRB jet breaks will likely be detectable by current capabilities, and the fraction is certainly less when accounting for gamma-ray localization by GBM, timing of afterglow observations, and other afterglow observational constraints. A previous study of *Swift* afterglows (Racusin et al. 2009) found strong evidence of a jet break in the X-ray afterglow for only 12% of GRBs and moderate evidence of a jet break for another 30%. A conclusion of that study was that at least 40% of afterglows with missing jet breaks are due to observational biases which agrees with the results of our analysis. Predicting the timing of the jet break without knowing the redshift by this method might not be practical either, since the t_j PDF for an individual GRB is quite broad, as shown in Figure 10(b). Knowledge of the redshift will help narrow the PDF, although the 1σ interval for predicting the jet break time will still usually be on the order of a few days.

4. Summary

In this paper we have described a method which can be used to estimate the jet opening angle of GRBs based on comparisons to estimates derived from observed jet breaks, even in cases where the redshift is not known. From the jet opening angle and redshift, the collimation-corrected energetics can be calculated. We have shown that the cosmologically calibrated Ghirlanda relation is a tight correlation between the time-integrated $E_{p,z}$ and E_γ , and the correlation slope matches the estimate from the theoretical predictions. By inverting the Ghirlanda relation, the jet opening angle can be estimated and is consistent with values inferred from observed jet breaks in the afterglow. This estimate requires the fluence in gamma rays, the observed peak of the νF_ν spectrum, and the redshift of the GRB. Furthermore, if the redshift is not known, we have shown that the modeled detector-dependent GRB redshift distribution can place constraints on θ_j and the rest-frame energetics of the GRB. We also note that the θ_j and energetics PDFs and distributions produced for GRBs without known redshift are not sensitive to moderate changes in cosmological assumptions or the GRB luminosity function, therefore we do not expect our results to change significantly with a moderately different assumptions.

Combining the estimates of θ_j from the described method and the inferred rest-frame energetics of 638 long GRBs detected by *Fermi* GBM in its first 4 years of operation, we have produced distributions of rest-frame quantities that should provide insight into the progenitor and emission properties of collapsars. We provide the parametrization of these distributions as well as our estimates of the energetics for all of the GRBs in our GBM sample. These estimates represent the apparent radiative energetics from the jet of the GRB, and we still require estimation of the energy conversion efficiency and the Lorentz factor of the outflow to place constraints on the total energy budget of the GRBs. Additionally, three observed correlations between the rest-frame E_{peak} and the rest-frame

energy were also shown. We find that the $E_{p,z} - E_{\text{iso}}$ correlation is roughly consistent with theoretical predictions based on simple jet dynamics and observing angle relative to the center of the jet. We also find that our fits to the $E_{p,z} - L_{\text{iso}}$ correlation is consistent with previous studies, however the slope for the $E_{p,z} - L_{\gamma}$ correlation is not consistent with the previous estimate of the slope by using GRBs with known redshift. This inconsistency may be attributable to the relatively small sample size and different fitting method employed in the previous study.

Finally, we have estimated the distribution of jet break times for GRBs and have shown that a large fraction of jet breaks are currently not observable, which places considerable constraints on the ability to directly infer the jet opening angle via an observed jet break. The jet break distribution has implications for follow-up observing strategies, future X-ray and optical detector sensitivities, and studying the many observational biases that may impact the non-detections of the jet breaks.

5. Acknowledgments

A.G. is funded by the NASA Postdoctoral Program through Oak Ridge Associated Universities.

REFERENCES

- Abdo, A. A. et al. 2009, *Science*, 323, 1688
- Abdo, A. A. et al. 2009, *ApJ*, 706, L138
- Amati, L. et al. 2002, *A&A*, 390, 81
- Amati, L. 2006, *MNRAS*, 372, 233
- Atteia, J. L. 2003, *A&A*, 407, L1
- Atteia, J. L. et al. 2005, *ApJ*, 626, 292
- Band, D. et al. 1993, *ApJ*, 413, 281
- Band, D. L. & Preece, R. D. 2005, *ApJ*, 627, 319
- Baring, M. G. & Braby, M. L. 2004, *ApJ*, 613, 460
- Bellm, E. C. et al. 2008, *ApJ*, 688, 491
- Bloom, J. S., Djorgovski, S. G., Kulkarni, S. R., & Frail, D. A. 1998, *ApJ*, 507, L25
- Bloom, J. S., Frail, D. A., & Sari, R. 2001, *ApJ*, 121, 2879
- Bloom, J. S., Frail, D. A., & Kulkarni, S. R. 2003, *ApJ*, 594, 674
- Burgess, J. M. et al. 2014, *ApJ*, 784, 17
- Cabrera, J. L., Firmani, C., Avila-Reese, V., Ghirlanda, G., Ghisellini, G., Nava, L. 2007, *MNRAS*, 382, 342
- Cenko, S. B. et al. 2011, *ApJ*, 732, 29
- Chandra, P. et al. 2009, *ApJ*, 683, 924

- Cobb, B. E., Bloom, J. S., Perley, D. A. et al. 2010, *ApJ*, 718, L150
- Collazzi, A. C., Schaefer, B. E., & Moree, J. A. 2011, *ApJ*, 729, 89
- Collazzi, A. C., Schaefer, B. E., Goldstein, A., & Preece, R. D. 2012, *ApJ*, 747, 39
- Costa, E. 1999, *A&AS*, 138, 425
- Coward, D. M., Howell, E. J., Brachesi, M., Stratta, G., Guetta, D., Gendre, B.,
Macpherson, D. 2013, *MNRAS*, 432, 2141
- Filgas, R. et al. 2011, *A&A*, 535, A57
- Frail, D. A. et al. 2001, *ApJ*, 562, L55
- Freedman, D. L. & Waxman, E. 2001, *ApJ*, 547, 922
- Ghirlanda, G., Ghisellini, G., & Lazzati, D. 2004, *ApJ*, 616, 331
- Ghirlanda, G., Ghisellini, G., & Firmani, C. 2005, *MNRAS*, 361, L10
- Ghirlanda, G., Ghisellini, G., Firmani, C., Celotti, A., & Bosnjak, Z. 2005, *MNRAS*, 360,
L45
- Ghirlanda, G., Nava, L., Ghisellini, G., & Firmani, C. 2007, *A&A*, 466, 127
- Ghirlanda, G. et al. 2013, *MNRAS*, 428, 1410
- Ghisellini, G., Lazzati, D., Rossi, E., & Rees, M. J. 2002, *A&A*, 389, L33
- Goldstein, A. 2012, in proceedings of "Gamma-Ray Bursts 2012 Conference" PoS(GRB
2012)082
- Goldstein, A. et al. 2012, *ApJS*, 199, 19
- Goldstein, A. et al. *ApJS*, 208, 21

Golenetskii, S. et al. 2006, GCN Circ, 5837

Golenetskii, S. et al. 2008, GCN Circ, 7482

Gomboc, A. et al. 2008, ApJ, 687, 443

Greiner, J. April 2015, GRBs Localized with BSAX or BATSE/RXTE or ASM/RXTE
or IPN or HETE or INTEGRAL or Swift or AGILE or Fermi/GLAST or MAXI,
<http://www.mpe.mpg.de/~jcg/grbgen.html>

Gruber, D. et al. 2014, ApJS, 211, 12

Guetta, D., Piran, T., & Waxman, E. 2005, ApJ, 619, 412

Guidorzi, C., Frontera, F., Montanari, E., Rossi, F., Amati, L., Gomboc, A., &
Mundell, C. G. 2006, MNRAS, 371, 843

Harrison, F. A. et al. 1999, ApJ, 523, L121

Howell, E. J. & Coward, D. M. 2013, MNRAS, 428, 167

Hurkett, C. P. et al. 2006, MNRAS, 368, 1101

Jimenez, R., Band, D., & Piran, T. 2001, ApJ, 561, 171

Kelly, B. C. 2007, ApJ, 665, 1489

Kumar, P. & Piran, T. 2000, ApJ, 535, 152

Levinson, A. & Eichler, D. 2005, ApJ, 629, L13

Liang, E. W. & Dai, Z. G. 2004, ApJ, 608, L9

Liang N., Xiao, W., Liu, Y., Zhang, S. 2008, ApJ, 685, 384

- Mallozzi, R. S.m Paciesas, W. S., Pendleton, G. N., Briggs, M. S., Preece, R. D.,
Meegan, C. A., & Fishman, G, J. 1995, ApJ, 454 597
- Maselli, A. et al. 2014, Science, 343, 48
- Nakar, E. & Piran, T. 2005, MNRAS, 360, L73
- Nava, L. et al. 2012, MNRAS, 421, 1256
- Norris, J. P., Marani, G. F., & Bonnell, J. T. 2000, ApJ., 534, 248
- O'Brien, P. T. et al. 2006, ApJ, 647, 1213
- Page, K. L. et al. 2007, ApJ, 663, 1125
- Page, K. L. et al. 2011, MNRAS, 416, 2078
- Perley, D., A. et al. 2008, ApJ, 672, 449
- Racusin, J. L. et al. 2008, Nature, 455, 183
- Racusin, J. L. et al. 2009, ApJ, 698, 43
- Riess A. et al. 2011, ApJ, 730, 119
- Salvaterra, R. & Chincarini, G. 2007, ApJ, 656, L49
- Sari, R., Piran, T., & Halpern, J. P. 1999, ApJ, 519, L17
- Schaefer, B. E. 2003, ApJ, 583, L71
- Schaefer, B. E. 2007, ApJ, 660, 16
- de Ugarte Postigo, A., Goldoni, P., Milvang-Jensen, B., et al. 2011, GCN Circ, 11579
- Waxman, E. 1997, ApJ, 485, L5

Wijers, R. A. M. J. & Galama, T. J. 1999, *ApJ*, 523, 177

Yonetoku, D., Murakami, T., Nakamura, T., Yamazaki, R., Inoue, A. K, & Ioka, K. 2004,
ApJ, 609, 935

Zhang, B. et al. 2007, *ApJ*, 655, 989

Zhi-Ping, J. et al. 2013, *ApJ*, 774, 114

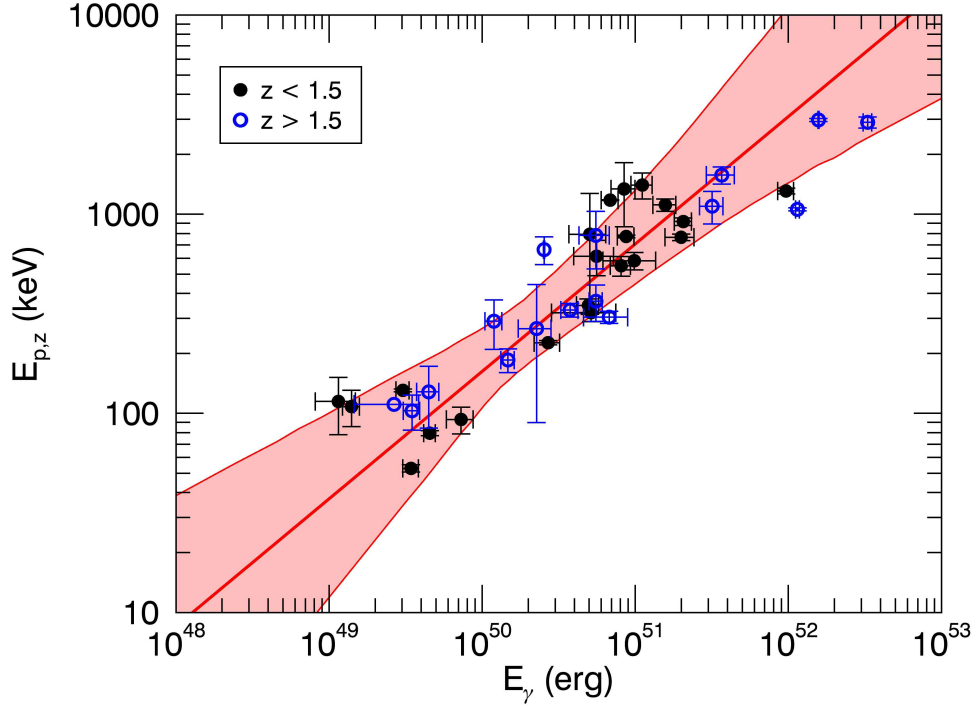


Fig. 1.— The Ghirlanda correlation between time-integrated E_{peak} and the peak collimation-corrected energy in gamma rays with 1σ error bars. The black filled circles are the GRBs at $z < 1.5$ which are calibrated using SNe Ia, and the blue open circles are GRBs at $z > 1.5$ which are produced assuming the concordant cosmology. Only the low- z data were used to fit the power law, and the red region is the 99% credible region for the power law fit.

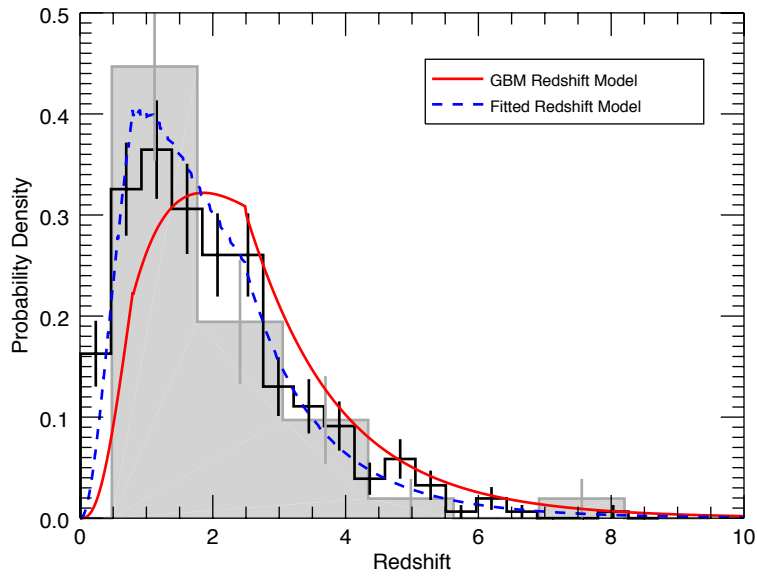


Fig. 2.— The distribution of spectroscopic redshift for 335 long GRBs through March 2015 (black), and the distribution of redshifts of 40 long GBM GRBs (shaded gray). The estimated redshift distribution of GRBs that can be triggered by GBM is shown in red. The blue dashed line is the same redshift distribution model fit to the observed distribution of GBM GRBs with redshift.

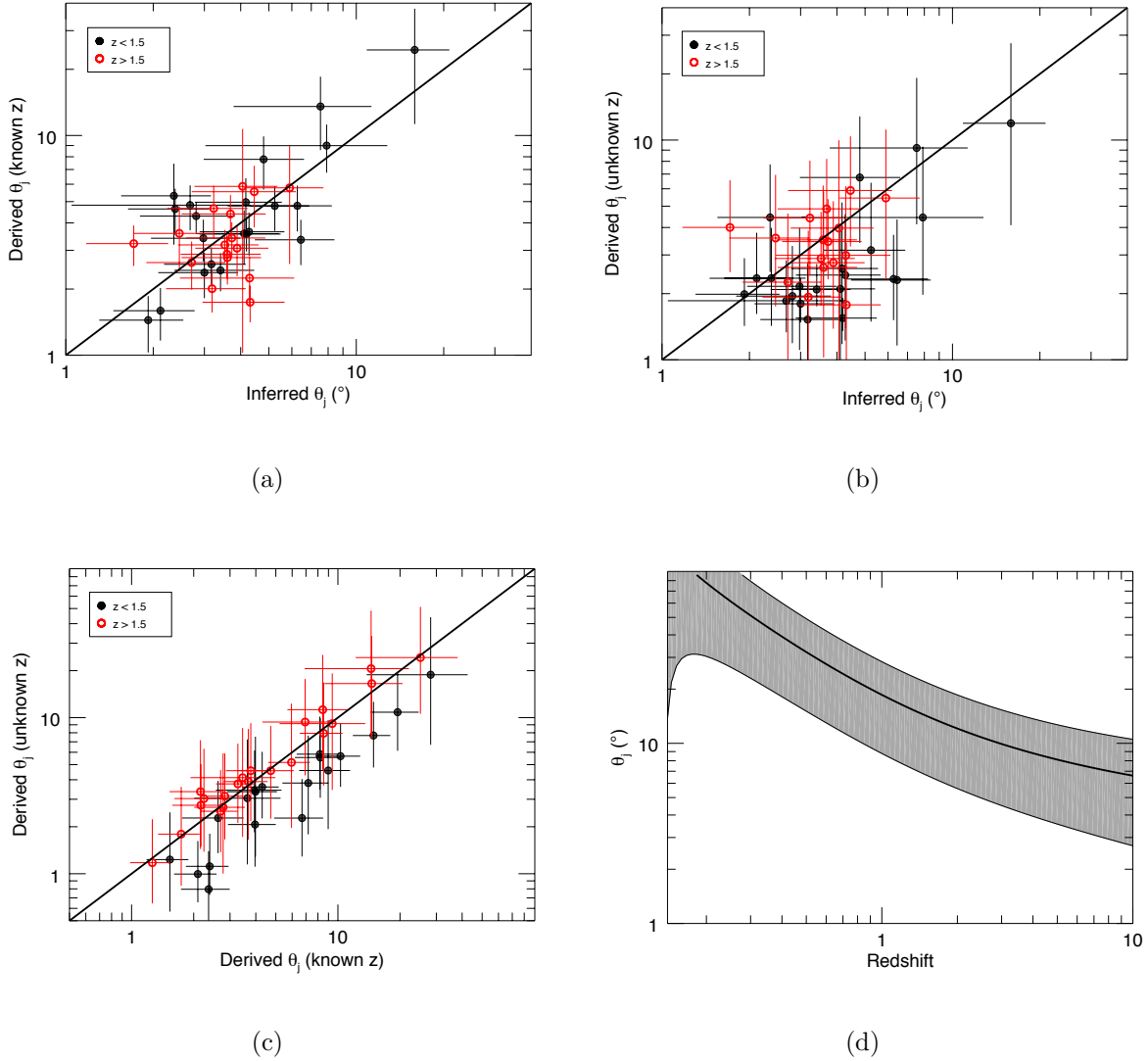
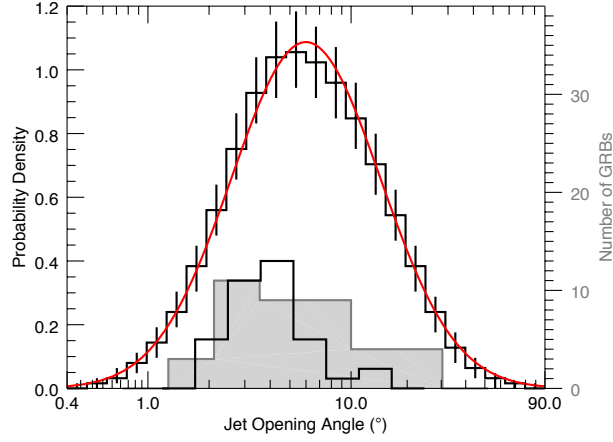
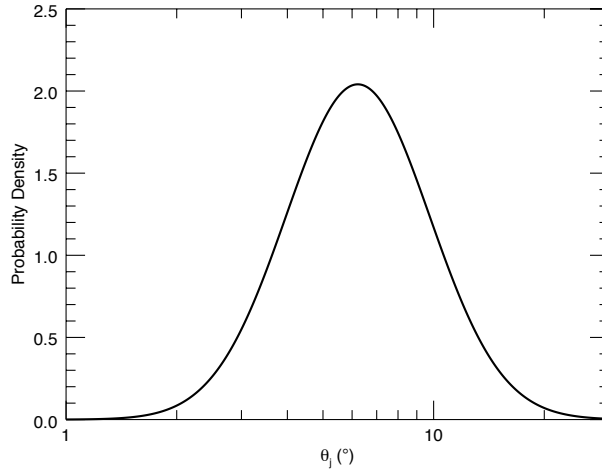


Fig. 3.— Panel 3(a) shows a comparison of the jet opening angle inferred from the afterglow jet break and the jet opening angle derived from the Ghirlanda relation. The black filled circles are the low-redshift calibration sample, and the red open circles are the high-redshift sample assuming Λ CDM. Panel 3(b) is a comparison of the jet opening angle inferred from the jet break and assuming the redshift is unknown. Panel 3(c) shows the estimation of θ_j for 40 long GRBs from the GBM catalog with observed redshift. Using the observed redshift to estimate θ_j is compared to assuming the GBM GRB redshift distribution. The systematic difference between GRBs with low- and high-redshifts can be explained by the functional dependence of θ_j on redshift, as shown in Panel 3(d), where higher redshift will tend to result in smaller θ_j for a fixed E_{peak} and fluence.

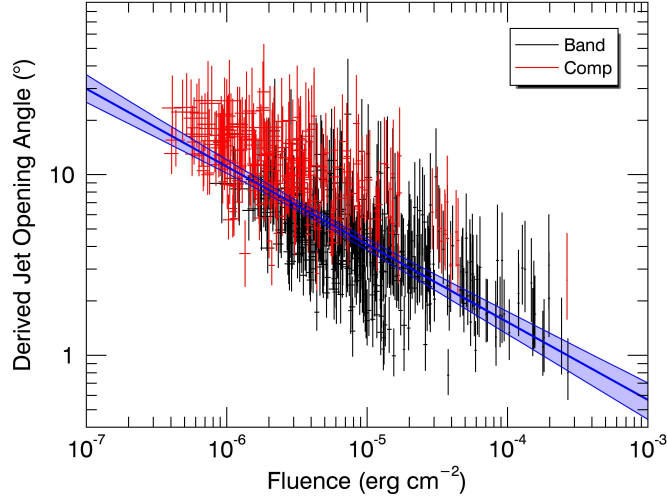


(a)

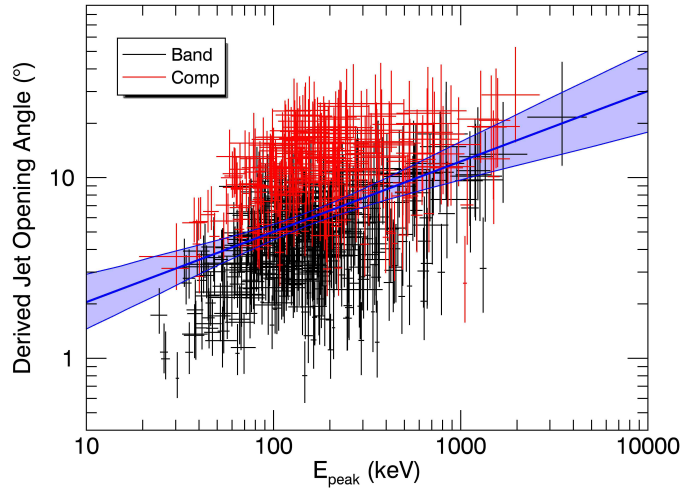


(b)

Fig. 4.— Panel 4(a) shows the distribution of derived jet opening angles for 638 GBM GRBs from the first 4 years of operation that are well fit by a Band function or a Comptonized function. The distribution peaks at ~ 6 degrees. The small black histogram represents the distribution of inferred angles from observed jet breaks, and the shaded histogram represents the distribution of derived angles from GBM GRBs with known redshift. Panel 4(b) shows a typical example of θ_j for a single GRB. In this example the 68% credible interval for θ_j is $4 - 10^\circ$.

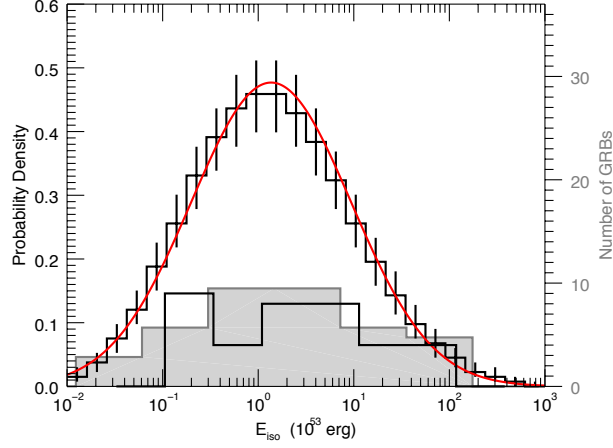


(a)

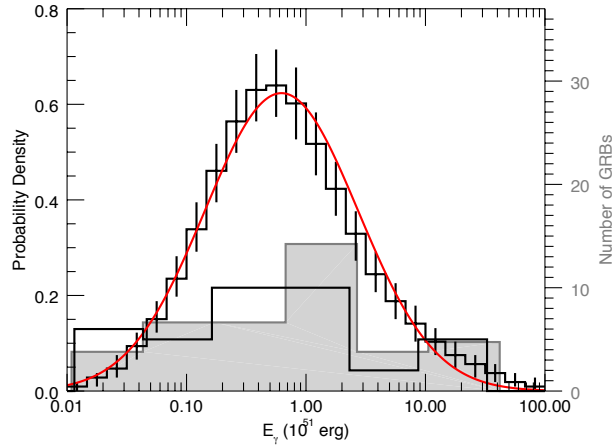


(b)

Fig. 5.— Panel 5(a) shows the dependence of the jet opening angle on GRB fluence. The blue region is the best fit power law regression, and if it is assumed to extend to lower fluence, a 90° opening angle would be likely at $\sim (5 - 10) \times 10^{-9}$ erg cm $^{-2}$. Panel 5(b) shows the dependence of the jet opening angle on the measured GRB E_{peak} . If the regression is assumed to extend to higher values of E_{peak} , a 90° opening angle would be likely at $\sim 60\text{--}700$ MeV.

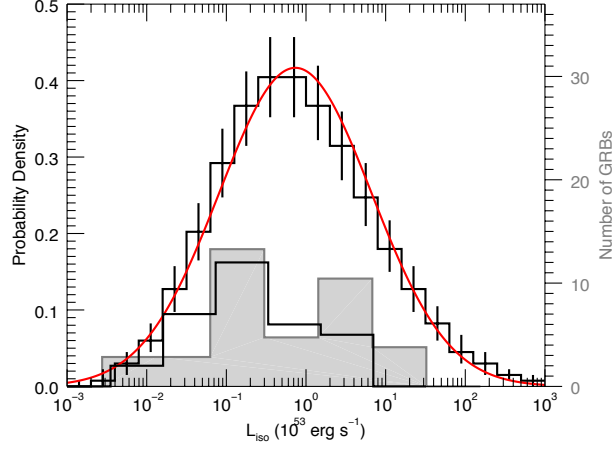


(a)

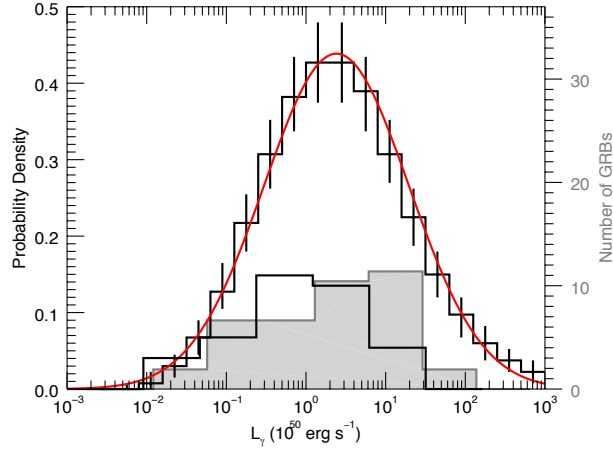


(b)

Fig. 6.— Panel 6(a) shows the distribution of the isotropic rest-frame energy in gamma rays, which peaks at $\sim 1 \times 10^{53}$ erg. Panel 6(b) shows the distribution of the collimation-corrected rest-frame energy in gamma rays. The distribution peaks at $\sim 6 \times 10^{50}$ erg. The small black histograms represent the distribution of measured E_{iso} and E_{γ} from the inferred jet opening angles, and the shaded histograms represent the distribution of derived E_{iso} and E_{γ} from GBM GRBs with known redshift.

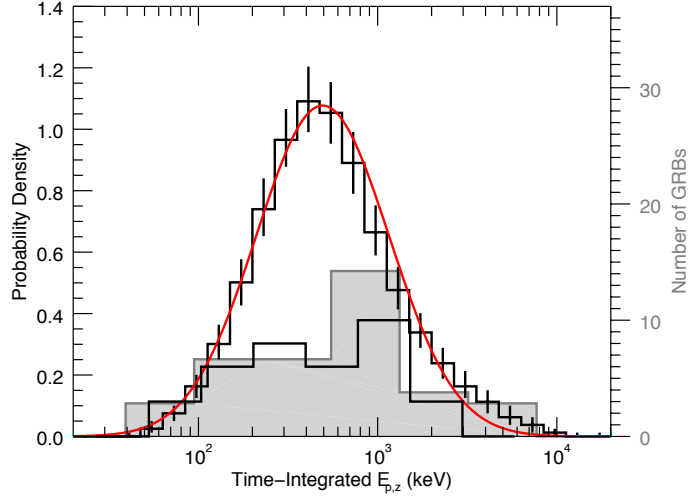


(a)

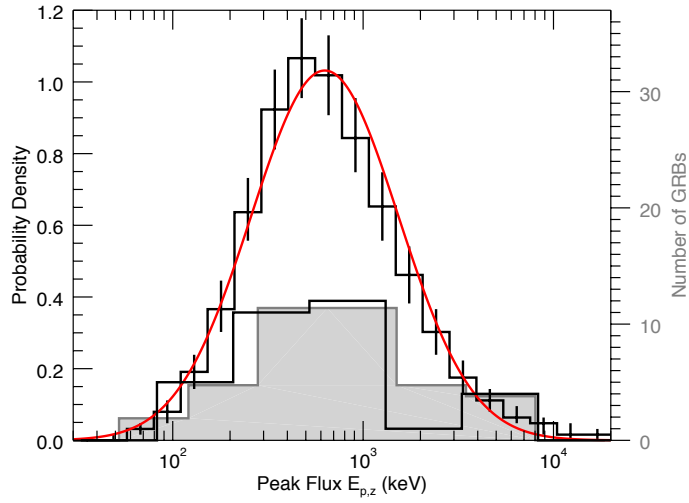


(b)

Fig. 7.— Panel 7(a) shows the distribution of the isotropic rest-frame peak luminosity (derived from the 1 s observed peak flux) in gamma rays, which peaks at $\sim 8 \times 10^{52} \text{ erg s}^{-1}$. Panel 7(b) shows the distribution of the collimation-corrected rest-frame peak luminosity in gamma rays. The distribution peaks at $\sim 2 \times 10^{50} \text{ erg s}^{-1}$. The small black histograms represent the distribution of measured L_{iso} and L_{γ} from the inferred jet opening angles, and the shaded histograms represent the distribution of derived L_{iso} and L_{γ} from GBM GRBs with known redshift.



(a)



(b)

Fig. 8.— Distribution of estimated rest-frame E_{peak} . The time-integrated $E_{p,z}$ peaks at ~ 500 keV, and the peak flux $E_{p,z}$ peaks at ~ 600 keV. The small black histograms represent the distributions of observed $E_{p,z}$ from the jet break sample, and the shaded histograms represent the distribution of derived $E_{p,z}$ from GBM GRBs with known redshift.

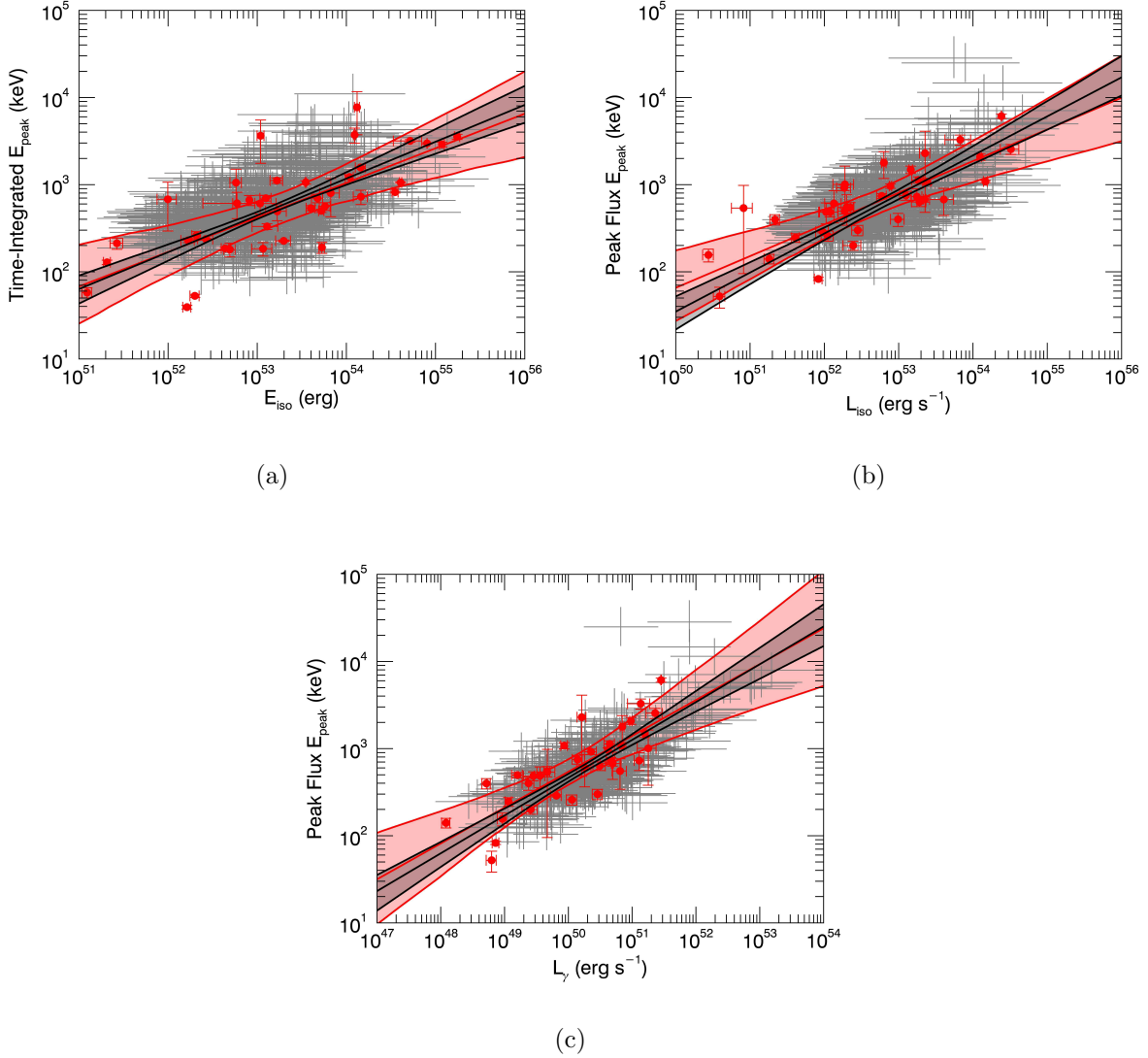
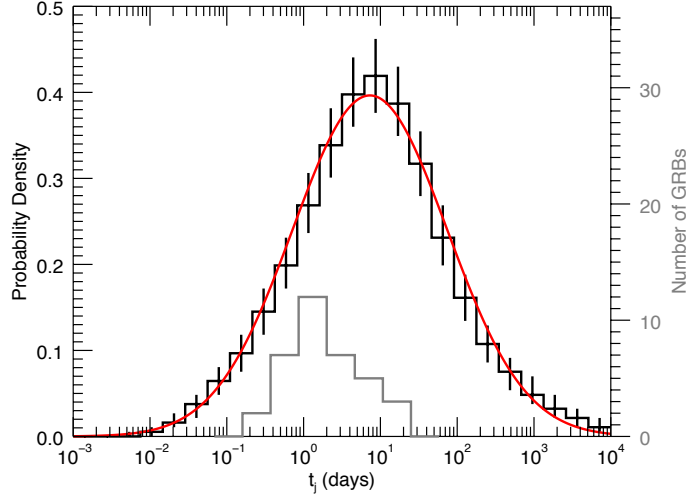
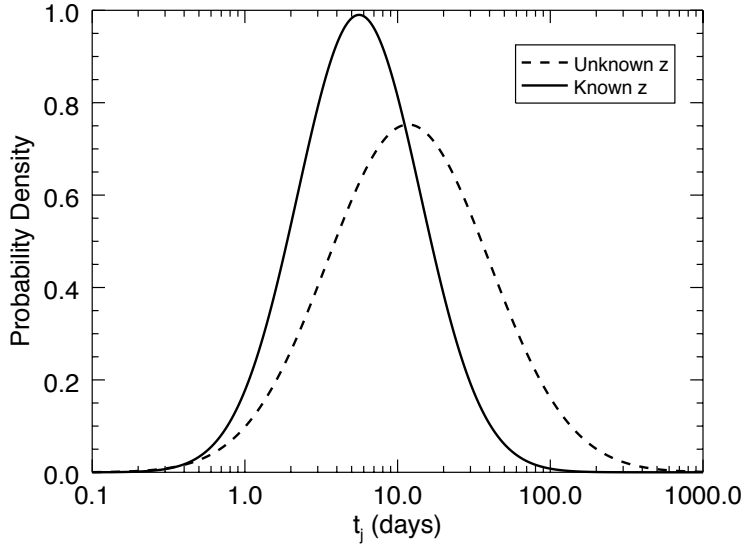


Fig. 9.— The (a) $E_{p,z} - E_{\text{iso}}$, (b) $E_{p,z} - L_{\text{iso}}$, and (c) $E_{p,z} - L_{\gamma}$ correlations using the GBM sample. The error bars denote the 68% credible regions for each data point. The gray regions are the 99% credible regions for the power-law fits to the large population of GRBs with unknown redshift (gray points), and the red regions are the 99% credible regions for the power-law fits to the GBM GRBs with known redshift (red points).



(a)



(b)

Fig. 10.— Panel 10(a) shows the distribution of the estimated jet break time. The distribution peaks at ~ 7 days. The gray histogram represents the distribution of observed jet break times from the afterglow. Panel 10(b) shows a typical example of the t_j PDF for a single GRB with known z (68% credible region of 6–14 days), and a typical t_j PDF for a different GRB with unknown z (68% credible region of 4–42 days).

Table 1. GRB parameters used to calculate jet opening angle ($z < 1.5$)

| GRB | z | t_j (days) | α | β | E_{peak} (keV) | Fluence (10^{-6} erg cm^{-2}) | Band (keV) | Ref. [†] |
|---------|------|-------------------|------------------|------------------|----------------------------|---|---------------|-------------------|
| 970508 | 0.83 | $25.0 \pm 5.0^*$ | -1.24 ± 0.17 | -1.81 ± 0.20 | 432.6 ± 261.2 | 3.56 ± 0.25 | 20–2000 | 1,2 |
| 970828 | 0.96 | 2.20 ± 0.40 | -0.74 ± 0.01 | -2.07 ± 0.40 | 298.0 ± 30.0 | 96.0 ± 10.0 | 20–2000 | 1,3 |
| 980703 | 0.97 | $3.40 \pm 0.50^*$ | -1.20 ± 0.05 | -1.93 ± 0.06 | 280.1 ± 31.7 | 39.8 ± 0.90 | 20–2000 | 1,2 |
| 990705 | 0.84 | 1.00 ± 0.20 | -1.05 ± 0.21 | -2.20 ± 0.10 | 189.0 ± 15.0 | 75.0 ± 8.0 | 40–700 | 4 |
| 990712 | 0.43 | 1.60 ± 0.30 | -1.88 ± 0.07 | -2.48 ± 0.56 | 65.0 ± 10.0 | 6.50 ± 0.30 | 40–700 | 5,4 |
| 991216 | 1.02 | 1.20 ± 0.40 | -1.20 ± 0.01 | -2.22 ± 0.02 | 382.4 ± 5.9 | 174 ± 0.53 | 20–2000 | 1,2 |
| 010222 | 1.48 | 0.93 ± 0.10 | -1.35 ± 0.19 | -1.64 ± 0.02 | 309.0 ± 12.0 | 93.0 ± 3.00 | 40–700 | 4 |
| 020405 | 0.69 | 1.67 ± 0.52 | -1.10 ± 0.40 | -1.87 ± 0.23 | 364.0 ± 73.0 | 74.0 ± 7.00 | 15–2000 | 5,4 |
| 020813 | 1.25 | 0.43 ± 0.06 | -0.94 ± 0.03 | -2.30 ± 0.50 | 142.0 ± 14.0 | 98.0 ± 1.00 | 2–400 | 4 |
| 030329 | 0.17 | 0.50 ± 0.10 | -1.26 ± 0.02 | -2.28 ± 0.05 | 68.0 ± 2.0 | 163 ± 1.40 | 2–400 | 4 |
| 041006 | 0.72 | 0.16 ± 0.04 | -1.37 ± 0.10 | – | 63.0 ± 13.0 | 12.0 ± 1.00 | 2–400 | 4 |
| 050318 | 1.44 | $0.21 \pm 0.07^*$ | -0.34 ± 0.32 | – | 47.0 ± 15.0 | 2.10 ± 0.20 | 15–350 | 4 |
| 050525 | 0.61 | 0.28 ± 0.12 | -1.01 ± 0.06 | -3.26 ± 0.20 | 81.2 ± 1.4 | 20.0 ± 1.00 | 15–350 | 4 |
| 051022 | 0.80 | $2.90 \pm 0.20^*$ | -1.18 ± 0.02 | – | 510.0 ± 22.0 | 261 ± 9.00 | 20–2000 | 4 |
| 061121 | 1.31 | 2.31 ± 1.16 | -1.32 ± 0.05 | – | 606.0 ± 90.0 | 56.7 ± 5.00 | 20–5000 | 6, 7 |
| 061126 | 1.16 | 6.75 ± 5.25 | -1.06 ± 0.07 | -2.7 ± 0.40 | 620.0 ± 220.0 | 30.0 ± 4.00 | 15–10000 | 8,9 |
| 080319B | 0.94 | 0.03 ± 0.01 | -0.86 ± 0.01 | -3.59 ± 0.62 | 675.0 ± 22.0 | 613 ± 13.0 | 20–7000 | 10 |
| 090328 | 0.74 | 6.40 ± 6.0 | -1.09 ± 0.02 | -2.37 ± 0.18 | 639.7 ± 45.7 | 50.9 ± 0.82 | 10–1000 | 11,12 |
| 090618 | 0.54 | 0.60 ± 0.05 | -1.13 ± 0.01 | -2.22 ± 0.02 | 146.9 ± 3.6 | 257 ± 1.50 | 10–1000 | 13,12 |
| 091127 | 0.49 | 0.38 ± 0.04 | -1.26 ± 0.07 | -2.22 ± 0.02 | 35.5 ± 1.5 | 18.3 ± 0.21 | 10–1000 | 14,12 |
| 130427A | 0.34 | 0.43 ± 0.40 | -0.91 ± 0.01 | -3.18 ± 0.03 | 877.8 ± 4.9 | 1900 ± 2.0 | 10–1000 | 15 |

The β column contains the Band function high-energy power-law index. The α column contains the Band function low-energy power-law index unless the corresponding β values is missing. In this case, α represents the spectral index from the Comptonized function.

* Either optical afterglow observations were unavailable or unable to constrain jet break time; X-ray break only.

† The first number references the jet break time source, and the second number references the spectral parameters source.

When there is just one number, the same source is used for the jet break time and the spectral parameters. 1-Bloom et al. (2003); 2-Goldstein et al. (2013); 3-Jimenez et al. (2001); 4-Schaefer (2007); 5-Ghirlanda et al. (2004); 6-Page et al. (2007); 7-Golenetskii et al. (2006); 8-Gomboc et al. (2008); 9-Perley et al. (2008); 10-Racusin et al. (2008); 11-Cenko et al. (2011); 12-Goldstein et al. (2012b); 13-Page et al. (2011); 14-Filgas et al. (2011); 15-Maselli et al. (2014)

Table 2. GRB parameters used to calculate jet opening angle ($z > 1.5$)

| GRB | z | t_j (days) | α | β | E_{peak} (keV) | Fluence (10^{-6} erg cm^{-2}) | Band (keV) | Ref. † |
|---------|------|-------------------|------------------|------------------|----------------------------|---|---------------|--------|
| 990123 | 1.60 | 2.04 ± 0.46 | -0.90 ± 0.10 | -2.48 ± 0.40 | 604.0 ± 60.0 | 270 ± 30.0 | 20–2000 | 1 |
| 990510 | 1.62 | 1.60 ± 0.20 | -1.28 ± 0.10 | -2.67 ± 0.40 | 126.0 ± 10.0 | 23.0 ± 2.00 | 20–2000 | 1 |
| 000926 | 2.04 | 1.80 ± 0.10 | -1.10 ± 0.10 | -2.43 ± 0.40 | 100.0 ± 7.0 | 6.20 ± 0.60 | 25–100 | 2,1 |
| 011211 | 2.14 | 1.56 ± 0.16 | -0.84 ± 0.09 | – | 59.0 ± 8.0 | 5.00 ± 0.50 | 40–700 | 1 |
| 020124 | 3.20 | 3.00 ± 0.40 | -0.79 ± 0.15 | – | 87.0 ± 18.0 | 8.10 ± 0.80 | 2–400 | 1 |
| 021004 | 2.33 | 4.74 ± 0.50 | -1.01 ± 0.18 | – | 80.0 ± 53.0 | 2.50 ± 0.60 | 2–400 | 1 |
| 030226 | 1.99 | 1.04 ± 0.12 | -0.89 ± 0.16 | – | 97.0 ± 27.0 | 5.60 ± 0.70 | 2–400 | 1 |
| 030328 | 1.52 | 0.80 ± 0.10 | -0.80 ± 0.80 | -2.30 ± 0.00 | 44.0 ± 44.0 | 0.65 ± 0.28 | 50–300 | 1,3 |
| 030429 | 2.66 | 1.77 ± 1.00 | -1.12 ± 0.24 | – | 35.0 ± 12.0 | 0.85 ± 0.14 | 2–400 | 1 |
| 050505 | 4.27 | $0.67 \pm 0.14^*$ | -0.95 ± 0.31 | – | 125.9 ± 20.0 | 15.8 ± 0.16 | 15–350 | 4,5 |
| 060124 | 2.30 | $1.10 \pm 0.10^*$ | -1.29 ± 0.07 | -2.25 ± 0.30 | 237.0 ± 76.0 | 28.0 ± 3.00 | 20–2000 | 1 |
| 060526 | 3.12 | 1.27 ± 0.35 | -1.10 ± 0.40 | – | 25.0 ± 5.0 | 0.49 ± 0.06 | 15–150 | 1 |
| 070125 | 1.55 | 3.80 ± 0.10 | -1.13 ± 0.09 | -2.08 ± 0.14 | 430.0 ± 80.0 | 179 ± 13.0 | 20–10000 | 6,7 |
| 090323 | 3.57 | $17.6 \pm 11.2^*$ | -1.29 ± 0.01 | -2.44 ± 0.17 | 632.9 ± 40.8 | 128 ± 1.50 | 10–1000 | 8,9 |
| 090902B | 1.82 | 6.20 ± 0.80 | -1.01 ± 0.01 | – | 1054 ± 17.4 | 266 ± 0.77 | 10–1000 | 8,9 |
| 090926A | 2.11 | 9.00 ± 2.00 | -0.86 ± 0.01 | -2.40 ± 0.04 | 340.0 ± 5.7 | 154 ± 7.20 | 10–1000 | 8,9 |

The β column contains the Band function high-energy power-law index. The α column contains the Band function low-energy power-law index unless the corresponding β values is missing. In this case, α represents the spectral index from the Comptonized function.

* Either optical afterglow observations were unavailable or unable to constrain jet break time; X-ray break only.

† The first number references the jet break time source, and the second number references the spectral parameters source.

When there is just one number, the same source is used for the jet break time and the spectral parameters. 1-Schaefer (2007); 2-Bloom et al. (2003); 3-Atteia et al. (2005); 4-Hurkett et al. (2006); 5-Cabrera et al. (2007); 6-Chandra et al. (2008); 7-Bellm et al. (2008); 8-Cenko et al. (2011); 9-Goldstein et al. (2012b)

Table 3. Log-normal distribution parameters.

| Quantity | μ | σ |
|------------------|------------------|-----------------|
| θ_j | 0.77 ± 0.02 | 0.37 ± 0.01 |
| E_{iso} | 0.14 ± 0.04 | 0.84 ± 0.03 |
| E_γ | -0.21 ± 0.03 | 0.64 ± 0.03 |
| L_{iso} | -0.13 ± 0.06 | 0.96 ± 0.05 |
| L_γ | 0.38 ± 0.06 | 0.91 ± 0.05 |
| $E_{p,z}$ | 2.69 ± 0.02 | 0.37 ± 0.02 |
| $E_{p,z}$ (peak) | 2.80 ± 0.02 | 0.39 ± 0.02 |
| t_j | 0.86 ± 0.05 | 1.00 ± 0.05 |

Table 4. Jet Angle and Energetics PDFs Table Format

| Column | Format | Description |
|--------|--------|--|
| 1 | A9 | GBM Trigger # |
| 2 | F5.2 | θ_j log-normal mean |
| 3 | F4.2 | θ_j log-normal std. dev. |
| 4 | F5.2 | E_{iso} log-normal mean |
| 5 | F4.2 | E_{iso} log-normal std. dev. |
| 6 | F5.2 | E_γ log-normal mean |
| 7 | F4.2 | E_γ log-normal std. dev. |
| 8 | F5.2 | L_{iso} log-normal mean |
| 9 | F4.2 | L_{iso} log-normal std. dev. |
| 10 | F5.2 | L_γ log-normal mean |
| 11 | F4.2 | L_γ log-normal std. dev. |
| 12 | F4.2 | Time-integrated $E_{p,z}$ log-normal mean |
| 13 | F4.2 | Time-integrated $E_{p,z}$ log-normal std. dev. |
| 14 | F4.2 | Peak $E_{p,z}$ log-normal mean |
| 15 | F4.2 | Peak $E_{p,z}$ log-normal std. dev. |
| 14 | F5.2 | t_j log-normal mean |
| 15 | F4.2 | t_j log-normal std. dev. |